Available online at www.sciencedirect.com
ScienceDirect
Comput. Methods Appl. Mech. Engrg. 333 (2018) 218–237
Computer methods in applied mechanics and engineering
www.elsevier.com/locate/cma

Stochastic time-optimal path-planning in uncertain, strong, and dynamic flows

Deepak N. Subramani*, Quantum J. Wei, Pierre F.J. Lermusiaux*

Department of Mechanical Engineering, Massachusetts Institute of Technology, 77 Massachusetts Avenue, Rm 5-207B, Cambridge, MA 02139, United States

Received 20 September 2017; accepted 3 January 2018
Available online 31 January 2018

Highlights

- S-PDEs governing reachability and time-optimality in uncertain, dynamic, strong flows.
- Derived efficient stochastic DO level-set equations for accurate and fast computation.
- Equations applied to a stochastic front, double-gyre QG flow, and flow past an island.
- Rigorous framework to quantify sensitivity of time-optimal paths to forecast errors.

Abstract

Accounting for uncertainty in optimal path planning is essential for many applications. We present and apply stochastic level-set partial differential equations that govern the stochastic time-optimal reachability fronts and time-optimal paths for vehicles navigating in uncertain, strong, and dynamic flow fields. To solve these equations efficiently, we obtain and employ their dynamically orthogonal reduced-order projections, maintaining accuracy while achieving several orders of magnitude in computational speed-up when compared to classic Monte Carlo methods. We utilize the new equations to complete stochastic reachability and time-optimal path planning in three test cases: (i) a canonical stochastic steady-front with uncertain flow strength, (ii) a stochastic barotropic quasi-geostrophic double-gyre circulation, and (iii) a stochastic flow past a circular island. For all the three test cases, we analyze the results with a focus on studying the effect of flow uncertainty on the reachability fronts and time-optimal paths, and their probabilistic properties. With the first test case, we demonstrate the approach and verify the accuracy of our solutions by comparing them with the Monte Carlo solutions. With the second, we show that different flow field realizations can result in paths with high spatial dissimilarity but with similar arrival times. With the third, we provide an example where time-optimal path variability can be very high and sensitive to uncertainty in eddy shedding direction downstream of the island.

Keywords: Stochastic path planning; Level set equations; Dynamically orthogonal; Ocean modeling; AUV; Uncertainty quantification

* Corresponding authors.
E-mail addresses: deepakns@mit.edu (D.N. Subramani), pierrel@mit.edu (P.F.J. Lermusiaux).

https://doi.org/10.1016/j.cma.2018.01.004
0045-7825/

1. Introduction

Planning optimal paths of autonomous platforms in dynamic environments such as the ocean and atmosphere is important for maximally utilizing the platforms' capabilities. In the ocean, commonly used autonomous vehicles – underwater gliders, propelled underwater vehicles and surface crafts – often undertake complex missions such as oceanographic data collection, search and rescue operations, oil and gas discovery, and acoustic surveillance and security tasks [1–3]. Path planning is the task of predicting paths for these vehicles to navigate between any two points while optimizing some or all operational parameters such as time, energy, data collected, and safety. A related concept is dynamic reachability forecasts, the task of predicting the dynamic set of all the locations that can be reached by these vehicles.

One major challenge in dynamic reachability forecasting and optimal path planning for realistic ocean conditions is that current forecasts are uncertain. There could be uncertainties in the initial conditions, boundary conditions, parameters and even terms in the equations themselves [4]. In the present paper, our objective is to develop fundamental and efficient stochastic equations and methodology for computing the reachability fronts and time-optimal paths of vehicles navigating in uncertain, strong, and dynamic flow fields. As we will see, such an approach also helps us in quantifying the sensitivity of optimal paths to errors in flow predictions.

A traditional focus of path planning has been on autonomous agents in complex but static environments. These traditional methods can be broadly grouped into graph-based search methods, nonlinear optimization methods including those with evolutionary algorithms, and dynamics-based approaches including Lagrangian Coherent Structures. For a review, see, e.g., [5–8], and references therein. Recently, fundamental level-set Partial Differential Equations (PDEs) that govern reachability have been developed for time-optimal [7,9,10] and energy-optimal [11] path planning of autonomous swarms in strong and dynamic deterministic flows. This level-set PDE-based methodology overcomes the limitations of traditional path planning methods designed for robotic motion in static environments. It can indeed directly utilize a prediction of the dynamic environment to plan time- or energy-optimal paths that intelligently utilize favorable flows and avoid adverse currents. It also directly avoids physical obstacles (e.g., islands) and forbidden regions due to operational constraints (e.g., minimum water depth) thereby ensuring vehicle safety. It has been employed to solve pursuit-evasion games in dynamic flows [12,13]. Its use with realistic deterministic ocean re-analyses was demonstrated in several ocean regions [14,15] and in real-time sea exercises with real AUVs [16]. However, the corresponding PDEs and methodology need to be extended to dynamic stochastic environments.

Progress has been made on path planning for autonomous robots in uncertain environments. Wellman et al. [17] extended graph-based search methods to account for uncertain edge costs with applications to stochastic bus networks. Kewlani et al. [18] extend graph-based algorithms to explicitly consider uncertainty in the mobility and terrain parameterizations using stochastic surface response methods. Potential field methods have been used in a Monte Carlo approach to solve path planning problems in uncertain flows by Barraquand and Latombe [19]. Rathbun et al. [20] report the use of evolutionary algorithms to plan paths of Unmanned Aerial Vehicles (UAV) in an airspace with uncertain obstacles. Wang et al. [21] perform path planning of autonomous vehicles in dynamic and uncertain ocean currents using an ensemble approach. The authors solve the deterministic Boundary Value Problem (BVP) for each member of the ensemble to compute the statistics of optimal trajectories. Considering all of these approaches, on the one hand, the extension of graph-based methods is not suitable for dynamic environments as their cost increases exponentially and there is a lack of optimality guarantee. On the other hand, the Monte Carlo and ensemble approaches can have slow convergence and prohibitive costs that increase with the complexity of uncertainty. For optimal path planning in dynamic stochastic environments, fundamental and efficient stochastic PDEs (S-PDEs) are needed.

In what follows, we first outline the problem statement, present our exact planning level-set S-PDEs and new efficient stochastic DO level-set PDEs (Section 2). Next, we showcase applications that validate and demonstrate the capabilities of our equations (Section 3). Finally, we provide some concluding remarks (Section 4).

2. Stochastic time-optimal planning PDEs

2.1. Problem statement

Consider an open set $\mathcal{D} \in \mathcal{R}^{n_\mathcal{D}}$ ($n_\mathcal{D} = 2$ or 3 for 2-D or 3-D in space), time $t \in [0, \infty)$ and a probability space $(\Omega, \mathcal{B}, \mathcal{P})$, where Ω is the sample space, $\mathcal{B}$ is the σ-algebra associated with Ω, and $\mathcal{P}$ is a probability measure. Starting at $t = 0$, let a vehicle (P) navigate in $\mathcal{D}$ from $\mathbf{x}_s$ to $\mathbf{x}_f$ with a nominal speed $F(\bullet) > 0$ under the influence of a

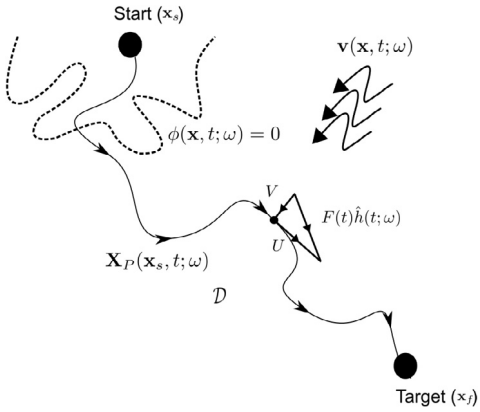

Fig. 1. *Schematic of stochastic time-optimal path planning setup:* Our goal is to compute the distribution of reachability fronts for vehicles starting from $\mathbf{x}_s$ in an uncertain flow field $\mathbf{v}(\mathbf{x}, t; \omega)$, and the distribution of time-optimal paths $\mathbf{X}_P(\mathbf{x}_s, t; \omega)$ to $\mathbf{x}_f$. The effective velocity, U experienced by the vehicle is the vector sum of the vehicle's forward motion $F(t)\hat{h}(t)$ and the background flow V.

stochastic dynamic flow-field $\mathbf{v}(\mathbf{x}, t; \omega) : \mathcal{D} \times [0, \infty)$, where $\omega \in \Omega$ is a random event. Let $\mathbf{X}_P(\mathbf{x}_s, t; \omega)$ be a general continuous trajectory from $\mathbf{x}_s$ to $\mathbf{x}_f$ (Fig. 1). The main notation is provided in Table 1.

Our goal is to predict the stochastic reachability fronts and time-optimal paths.

2.2. Stochastic level-set partial differential equations

We approach the above stochastic time-optimal path planning problem starting with the exact level-set PDEs for deterministic path planning [7]. Here, the source of stochasticity is the uncertain dynamic flow $\mathbf{v}(\mathbf{x}, t; \omega)$ (in comparison, the vehicle speed was artificially made stochastic for energy optimization in [11]). The stochastic reachability front for P is thus governed by the stochastic Hamilton–Jacobi (HJ) level-set equation

$$\frac{\partial \phi(\mathbf{x}, \mathbf{t}; \boldsymbol{\omega})}{\partial t} + F(t)|\nabla \phi(\mathbf{x}, t; \omega)| + \mathbf{v}(\mathbf{x}, t; \omega) \cdot \nabla \phi(\mathbf{x}, t; \omega) = 0\,, \tag{1}$$

with the initial condition $\phi(\mathbf{x}, 0; \omega) = |\mathbf{x} - \mathbf{x_s}|$ and, where needed, open boundary conditions such as $\left.\frac{\partial^2 \phi(\mathbf{x}, \mathbf{t}; \boldsymbol{\omega})}{\partial \mathbf{n}^2}\right|_{\delta\mathcal{D}} = 0$, where $\mathbf{n}$ is the outward normal to the boundary $\delta\mathcal{D}$, ω is a random event, and ϕ is the reachability-front-tracking scalar level-set field (e.g., signed distance function). For every ω, the optimal arrival-time $T^*(\mathbf{x}_f; \omega)$ at $\mathbf{x}_f$ is obtained by integrating Eq. (1) until the first time t such that $\phi(\mathbf{x}_f, t; \omega) \leq 0$. The corresponding optimal trajectory $\mathbf{X}_P^*(\mathbf{x}_s, t; \omega)$ is then given by the particle backtracking equation (where ϕ is differentiable)

$$\frac{d\mathbf{X}_P^*(\mathbf{x}_s, t; \omega)}{dt} = -\mathbf{v}(\mathbf{X}_P^*(\mathbf{x}_s, t; \omega), t; \omega) - F(t)\frac{\nabla \phi(\mathbf{X}_P^*(\mathbf{x}_s, t; \omega), t; \omega)}{|\nabla \phi(\mathbf{X}_P^*(\mathbf{x}_s, t; \omega), t; \omega)|},$$
$$0 \leq t \leq T^*(\mathbf{x}_f; \omega) \text{ and } \mathbf{X}_P^*(\mathbf{x}_s, T^*; \omega) = \mathbf{x}_f\,. \tag{2}$$

Solving the S-PDEs (1) and (2) would fulfill our goal. Eq. (1) can be integrated by direct Monte Carlo methods; however, the computational cost of such a method is prohibitive for practical applications. Classic reduced-order stochastic methods could be utilized [22–25]. However, due to the variable propulsion and advection terms, and the highly dynamic flows, they can sometimes diverge or be inefficient. We thus employ a dynamic stochastic order reduction, specifically the Dynamically Orthogonal (DO) field equations [26,27] that were shown to be an instantaneously optimal reduction using differential geometry arguments [28]. Next, we obtain these efficient stochastic DO level-set equations.

2.3. Stochastic Dynamically Orthogonal level-set equations for uncertain flow fields

A brief overview of the DO theory is provided in Appendix A. As mentioned previously, in [11] we obtained the stochastic DO level-set equations when the vehicle-speed $F(t)$ in Eq. (1) was made stochastic (i.e., $F(t) \to F(t; \omega)$).

Table 1
Relevant notation.

i, j	$\in\mathbb{N}$	Stochastic subspace index
F	$\in\mathbb{R}^+$	Vehicle speed
$\mathcal{D}$	$\in\mathbb{R}^{n_\mathcal{D}}$	Physical domain
$n_\mathcal{D}$	$\in\mathbb{N}$	Dimension of $\mathcal{D}$
n_x and n_y	$\in\mathbb{N}$	Number of discrete grid points in the x-direction and y-direction
n_g	$\in\mathbb{N}$	Total number of discrete grid points in $\mathcal{D}$
$n_{s,\phi}$	$\in\mathbb{N}$	Dimension of the stochastic subspace of ϕ, the level-set scalar field
$n_{s,\mathbf{v}}$	$\in\mathbb{N}$	Dimension of the stochastic subspace of $\mathbf{v}$, the velocity vector field
Y_i	$\in\mathbb{R}$	Random variable describing the PDF of the orthonormal level-set (ϕ) modes $\tilde{\phi}_i$
μ_i	$\in\mathbb{R}$	Random variable describing the PDF of the orthonormal velocity ($\mathbf{v}$) modes, $\tilde{\mathbf{v}}_i$
n_r	$\in\mathbb{N}$	Number of Monte Carlo realizations of the level-sets (and velocity vector fields)
r	$\in\mathbb{N}$	Realization index
$\mathbf{v}$	$\in\mathbb{R}^{n_\mathcal{D} n_g}$	Velocity vector field
$\bar{\mathbf{v}}$	$\in\mathbb{R}^{n_\mathcal{D} n_g}$	Mean velocity vector field
$\tilde{\mathbf{v}}_i$	$\in\mathbb{R}^{n_\mathcal{D} n_g}$	DO mode i of $\mathbf{v}$: Dynamically orthogonal basis for the stochastic subspace of $\mathbf{v}$
ϕ	$\in\mathbb{R}^{n_g}$	Level-Set field
$\bar{\phi}$	$\in\mathbb{R}^{n_g}$	Mean Level-Set field
$\tilde{\phi}_i$	$\in\mathbb{R}^{n_g}$	DO mode i of ϕ: Dynamically orthogonal basis for the stochastic subspace of ϕ
$C_{Y_i Y_j}$	$n_{s,\phi} \times n_{s,\phi}$	Covariance matrix between Y_i and Y_j for $i, j = 1 \cdots n_{s,\phi}$
$C_{\mu_j Y_k}$	$n_{s,\mathbf{v}} \times n_{s,\phi}$	Covariance matrix between μ_j and Y_k for $j = 1 \cdots n_{s,\mathbf{v}}$ and $k = 1 \cdots n_{s,\phi}$
Ω		Sample space of uncertain velocity
$\mathcal{B}$		σ-algebra associated with Ω
$\mathcal{P}$		Probability measure that returns the probability of events in $\mathcal{B}$
$\mathbb{E}[\bullet]$	$\in\mathbb{R}^{n_g}$	Expectation operator returning the mean of $\bullet$
$\langle \bullet, \bullet \rangle$	$\in \mathbb{R}$	Spatial inner-product operator between any two fields
ω	$\in \Omega$	A random event
$\mathbf{x_s}, \mathbf{x_f}$	$\in \mathcal{D}$	Start and final target locations
$\mathbf{X}^*_p(\mathbf{x}_s, t; \omega)$	$\in \mathcal{D} \times [0, \infty)$	Stochastic time optimal path from $\mathbf{x}_s$ to $\mathbf{x}_f$ corresponding to the random event ω
$T^*(\mathbf{x}_f; \omega)$	$\in \mathbb{R}^+$	Optimal arrival time at target $\mathbf{x}_f$ corresponding to the random event ω

Here, the difference is that we have a deterministic $F(t)$ and the stochasticity comes from the uncertain flow-field $\mathbf{v}(\mathbf{x}, t; \omega)$. This stochastic flow-field can be computed before solving the stochastic level-set equations and considered as an *external forcing* to the S-PDE (1).

Let us introduce DO decompositions to the uncertain flow-field $\mathbf{v}$ and the stochastic level-set ϕ as

$$\mathbf{v}(\mathbf{x}, t; \omega) = \bar{\mathbf{v}}(\mathbf{x}, t) + \sum_{j=1}^{n_{s,\mathbf{v}}} \mu_j(t; \omega)\tilde{\mathbf{v}}_j(\mathbf{x}, t)\,, \tag{3}$$

$$\phi(\mathbf{x}, t; \omega) = \bar{\phi}(\mathbf{x}, t) + \sum_{i=1}^{n_{s,\phi}} Y_i(t; \omega)\tilde{\phi}_i(\mathbf{x}, t)\,, \tag{4}$$

where $\mu_j(t; \omega), \forall\, j = 1 \ldots n_{s,\mathbf{v}}$, and $Y_i(t; \omega), \forall\, i = 1 \ldots n_{s,\phi}$, are zero-mean stochastic processes that represent the generally complex probability density functions of the velocity and level-set fields respectively.

Henceforth, we drop the spatial and temporal variables in parenthesis for brevity of notation. We use repeated indices to indicate a summation over $n_{s,\mathbf{v}}$ velocity DO modes or $n_{s,\phi}$ level-set DO modes, as the case may be. We also define $\gamma \equiv |\nabla\phi|$.

Substituting Eqs. (3) and (4) in Eq. (1), we obtain

$$\frac{\partial\bar{\phi}}{\partial t} + Y_i\frac{\partial\tilde{\phi}_i}{\partial t} + \tilde{\phi}_i\frac{dY_i}{dt} = -F\gamma - (\bar{v} + \mu_j\tilde{v}_j)\cdot\nabla(\bar{\phi} + Y_i\tilde{\phi}_i)\,. \tag{5}$$

We then derive the mean equation by applying the expectation operator to Eq. (5), the coefficient equations by projecting Eq. (5) onto the modes $\tilde{\phi}_i$, and the mode equations by multiplying Eq. (5) with Y_i and then applying the expectation operator. We provide the detailed derivation in Wei [29]. The results are as follows:

$$\frac{\partial\bar{\phi}}{\partial t} = -\left[F\mathbb{E}[\gamma] + \bar{\mathbf{v}}\cdot\nabla\bar{\phi} + C_{\mu_j Y_i}\tilde{\mathbf{v}}_j\cdot\nabla\tilde{\phi}_i\right], \tag{6a}$$

$$\frac{dY_i}{dt} = -\left\langle F(\gamma - \mathbb{E}[\gamma]) + Y_k\bar{\mathbf{v}}\cdot\nabla\tilde{\phi}_k + \mu_j\tilde{\mathbf{v}}_j\cdot\nabla\bar{\phi} + \tilde{\mathbf{v}}_j\cdot\nabla\tilde{\phi}_k(\mu_j Y_k - C_{\mu_j Y_k}), \tilde{\phi}_i\right\rangle, \tag{6b}$$

$$\frac{\partial\tilde{\phi}_i}{\partial t} = Q_i - \left\langle Q_i, \tilde{\phi}_n\right\rangle\tilde{\phi}_n\,, \tag{6c}$$

$$\text{where } Q_i = -C^{-1}_{Y_jY_i}\left[F\mathbb{E}[Y_j\gamma] + C_{Y_j\mu_k}\tilde{\mathbf{v}}_k\cdot\nabla\bar{\phi} + \mathbb{E}[Y_j\mu_kY_i]\tilde{\mathbf{v}}_k\cdot\nabla\tilde{\phi}_i\right] - \bar{\mathbf{v}}\cdot\nabla\tilde{\phi}_i\,,$$

where C denotes the covariance matrix between the two stochastic variables indicated in the respective subscripts (Table 1).

Here, we do not consider a separate DO decomposition for the non-polynomial nonlinearity γ but choose to handle only that term realization-by-realization and compute the required statistical quantities $\mathbb{E}[\gamma]$ and $\mathbb{E}[z\gamma]$. Other approaches for handling the non-polynomial nonlinearity, viz., *KL-Gamma* and *Taylor-Gamma* [11] could also be utilized (not shown here).

The solution of DO Eqs. (6) provides reachability fronts for all realizations ω. The minimum arrival time for each realization is the first time t for which $\phi(\mathbf{x}_f, t; \omega) \leq 0$. Subsequently, the stochastic particle backtracking Eq. (2) can be solved to obtain the time-optimal trajectories $\mathbf{X}^*_P(\mathbf{x}_s, t; \omega)$. The solution also provides the time-series of time-optimal headings $\hat{h}^*(t; \omega)$, again for all ω. In Section 3, we validate the solution obtained by the DO level-set Eq. (6) by comparing it with that obtained from direct Monte Carlo (MC) methods. We also showcase applications for predicting the stochastic reachability fronts, sets, and time-optimal trajectories for vehicles navigating in uncertain flow-fields.

2.4. Computational costs

The computational cost of solving the level-set PDE (1) for ω fixed is commonly dominated by the cost of the advection term. Thus, the cost of a MC method scales with the number of realizations and grid points as $O(n_r n_g)$. The cost of solving the stochastic DO level-set equations is also often dominated by the advection terms (by the velocity mean and modes). This cost scales as $O((n_{s,\mathbf{v}} + 1)(n_{s,\boldsymbol{\phi}} + 1)n_g)$ and is independent of n_r. n_r only affects the cost of solving the coefficient Eq. (6b), which is simply an ODE independent of n_g. For typical values of n_g, n_r, $n_{s,\phi}$, and $n_{s,\mathbf{v}}$ of realistic applications, the computational speed-up can be several orders of magnitude.

3. Applications

We apply the efficient stochastic DO level-set PDEs to compute stochastic reachability fronts and time-optimal paths in three test cases. They correspond to different stochastic flow configurations: (i) a simple canonical steady front where only the strength of the flow is uncertain, (ii) a stochastic dynamic barotropic quasi-geostrophic double-gyre circulation, and (iii) a stochastic flow past a circular island. We employ the first test case to verify the solution of the DO equations by comparing it with its corresponding Monte Carlo (MC) solution. In all test cases, we describe and study the variability in reachability fronts and time-optimal paths. The numerical parameters are listed in Table 2.

3.1. Test Case 1: Stochastic steady-front with uncertain flow strength

The first test case is a canonical flow — a steady zonal jet with uncertain flow strength. In addition to being a good candidate for developing and testing numerical schemes, this flow scenario is commonly encountered in the ocean. For example, the crossing of a shelfbreak front [15] or of channels [16] can be idealized by this canonical flow. Hence,

Table 2
Numerical parameters for all three test cases (notation defined in Table 1).

Test Case	n_x	n_y	dx	dy	dt	n_r	$n_{s,\mathbf{v}}$	$n_{s,\phi}$
1	300	150	1	1	5e-2	2000	1	50
2	100	100	0.01	0.01	1e-5	5000	5	50
3	240	90	0.067	0.067	1e-2	10000	8	50

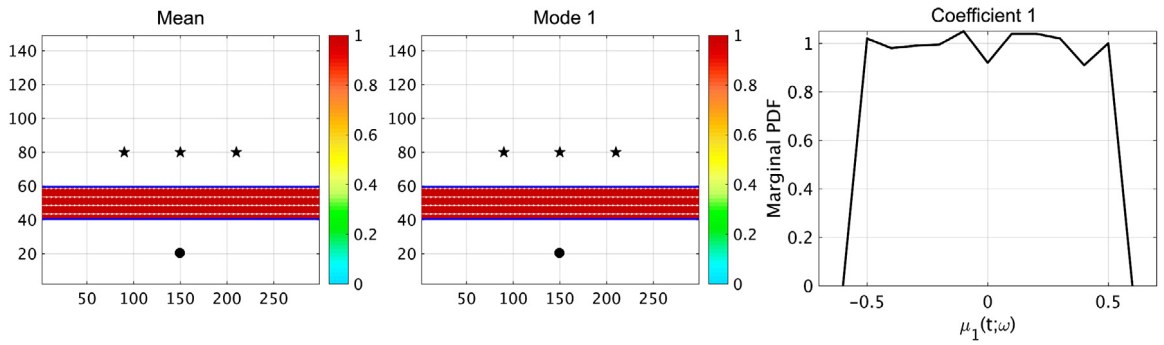

Fig. 2. *Mean, Mode, and PDF of coefficient for the DO decomposition of the velocity field used in Test Case 1:* The zonal jet is from West to East between $y = 40$ and $y = 60$, and has an uncertain strength of uniform density distribution with lower limit 0.5 and upper limit 1.5. The velocity is 0 elsewhere in the domain. The start point is marked with a circular marker and three end points with a star marker.

studying the properties of time optimal paths in such flows is a valuable first step for planning in realistic ocean flows later on.

The domain, flow configuration (mean, modes, and coefficients), and start and end points are provided in Fig. 2. The front is a steady jet flow from west to east, that is confined and constant in the region $40 < y < 60$. The strength of the flow is a random variable uniformly distributed from 0.5 to 1.5 within the jet proper. The flow is zero elsewhere in the domain. To represent the stochastic steady front with a uniformly distributed uncertain strength, we need only one DO mode for velocity, i.e., $n_{s,\mathbf{v}} = 1$. We utilize $n_r = 2{,}000$ realizations to represent the uniform PDF of flow strength (see Fig. 2a). We consider missions with a vehicle moving at a non-dimensional nominal speed of $F(t) = 1\,, \forall\, t = [0, \infty)$. The start point is (150,20) and the three targets are (90,80), (150,80), and (210,80). We compute the reachability fronts and sets by solving the stochastic DO level-set Eqs. (6), and time-optimal paths by solving the backtracking Eq. (2).

First, we verify the solution of Eqs. (6) by comparing it to the solution of Eq. (1) computed by the MC method. Then, we study the properties of the reachability fronts, sets and time-optimal paths.

3.1.1. Verification of the DO solution

To verify the DO solution, we first compute the corresponding MC solution and then compare the two. The MC solution is obtained by solving the level-set PDE for each of the n_r realizations of the velocity field separately. We look at the differences in arrival time at the target (210,80) and in the reachability front of all realizations. Fig. 3 shows the histogram of relative error in arrival time at the target (210,80). The arrival times computed by the DO

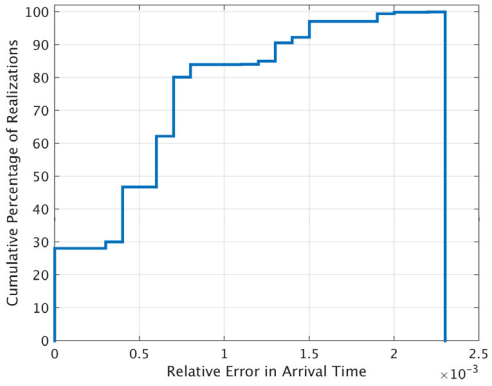

Fig. 3. *Cumulative histogram of relative error in arrival-time (between DO and MC solutions) for Test Case 1:* 82.80% realizations have a relative error in arrival-time (between the DO and MC solutions) of less than 0.0008 (0.1%), and the maximum relative error across all realizations is 0.0024 (0.24%). This error is negligible for the 4 orders of magnitude computational speed-up achieved by the DO level-set method.

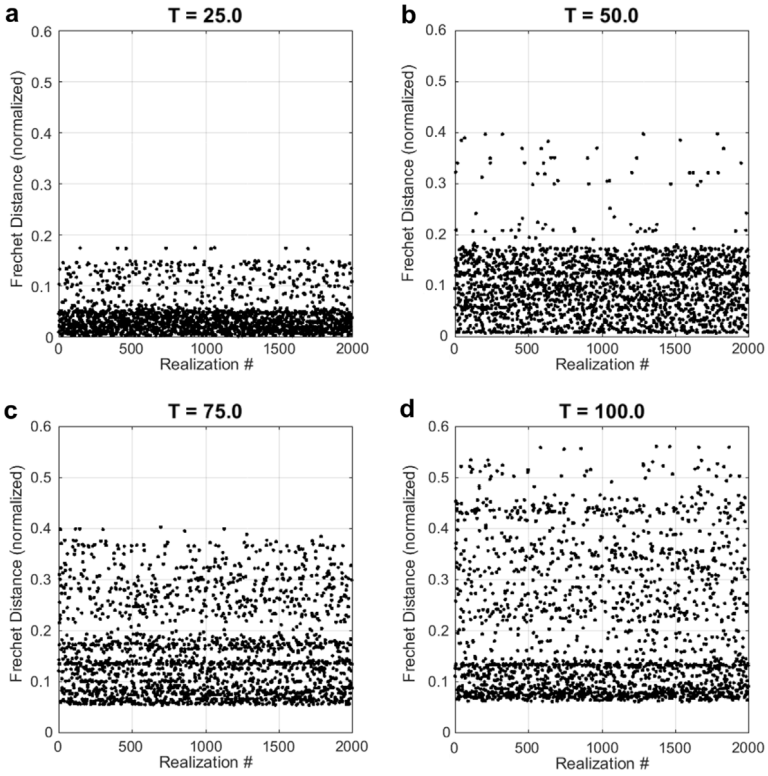

Fig. 4. *Frechet distance (normalized) between reachability fronts computed by the MC and DO methods for Test Case 1.* The difference between the reachability front computed by DO and MC increases with time, but always remains less than the spatial resolution. The difference can be further reduced by increasing the number of DO modes if the application requires higher precision. Frechet distances are normalized by grid spacing.

method are nearly identical to the corresponding times computed by the MC method. 26.55% of the realizations have zero error and 82.8% of realizations have less than 0.1% error in arrival times. The maximum error is 0.24%, which is 0.15 non-dimensional time or three discrete time-steps. Overall the error in arrival-time is negligible, especially considering that the DO method is 4 orders of magnitude faster than the MC method.

To quantify the difference in the reachability front, we utilize the discrete Frechet distance [11,30,31] which measures the maximum distance between two discrete curves in 2-D. Fig. 4 shows the discrete Frechet distance normalized by the grid spacing for all realizations, plotted at four non-dimensional times. All Frechet distances are less than the grid spacing, which indicates that the reachability front computed by the DO and MC methods are identical and the errors are less than or of the order of the spatial discretization. We also compared qualitatively by plotting the reachability fronts computed by both methods for some characteristic realizations and observed that DO and MC compute identical reachability fronts (not shown here, see [29]). We thus verified that the reachability front and arrival times computed using the DO level-set equations are accurate for our applications.

3.1.2. Analysis of stochastic reachability fronts and time-optimal paths

Fig. 5 shows the distribution of the stochastic reachability fronts computed by solving the stochastic DO level-set Eqs. (6). Each reachability front is colored with the flow strength of that realization. The six panels show snapshots of the spatial distribution of the reachability fronts at six non-dimensional times.

There is no uncertainty in the flow field outside the jet proper. Hence, the reachability fronts for all realizations are identical until the time when they first experience the uncertain flow. As shown in Fig. 5b, the part of the reachability fronts in the jet proper spreads out while the part that has not yet reached the jet remains identical for all realizations. As time progresses, the spread in the reachability fronts increases as each flow realization has a different flow strength

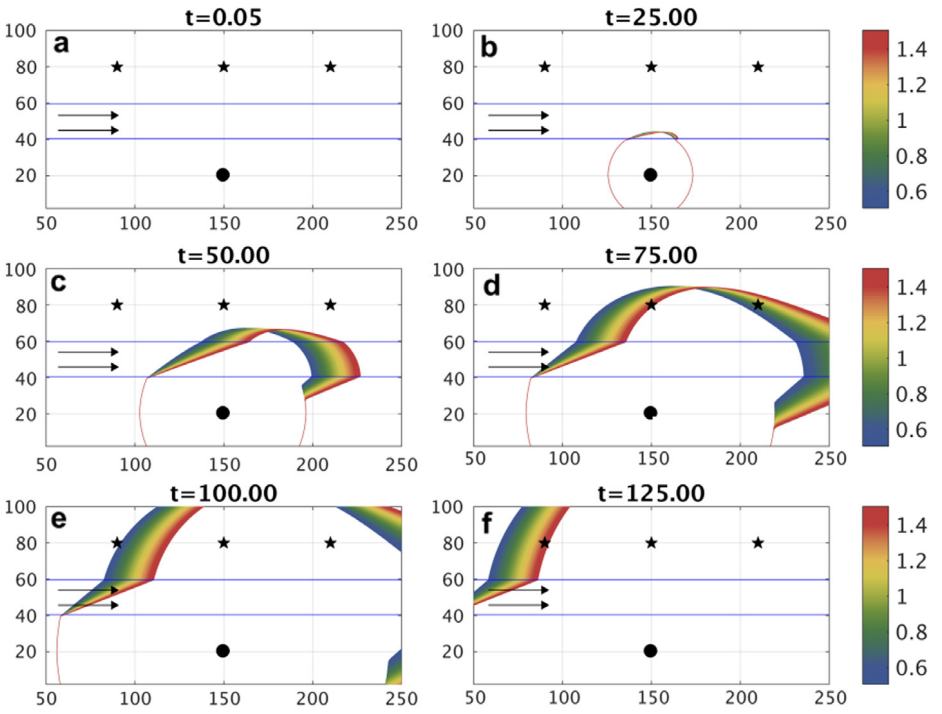

Fig. 5. *Stochastic reachability fronts for Test Case 1:* The reachability front for each of the flow realizations is colored with the strength of that flow realization.

(Fig. 5c–f). Most notably, there is a locus of points where pairs of reachability fronts corresponding to different flow realizations *cross-over* in Fig. 5c and d. For target points downstream of this locus of *cross-over* points, the higher the flow strength, the faster the vehicle arrives at the target. On the other hand, for target points upstream of this locus, the lower the flow strength of the stochastic jet, the faster the arrival-time at the target. In the former situation, the flow aids the motion of the vehicle to the target and thus stronger flows are favorable; however, in the latter situation, the flow hinders the motion of the vehicle to the target and thus weaker flows are favorable. By $t = 75$ (Fig. 5d), vehicles in all flow realizations have arrived at the target (150,80). By $t = 100$ (Fig. 5e), vehicles in all flow realizations have crossed the target (210,80) also and the reachability front of the weakest flow strength is just arriving at the target (90,80). By $t = 125$ (Fig. 5f), vehicles of almost all flow realizations have crossed (90,80).

Fig. 6 shows the stochastic time-optimal paths for all three targets. As before, each path is colored with the strength of the flow realization corresponding to that path. The spread of the paths increases progressively as the target moves upstream from the start point. The spatial distribution of the time-optimal paths to target (210,80) is narrow. In other words, the sensitivity of the time-optimal paths to errors in the flow field prediction is low. On the other hand, the spatial distribution of the time-optimal paths to (90,80) is wide. The sensitivity of the paths to errors in the flow field prediction is higher than the other two targets. For this test case, the more upstream the end point is, the larger the effect of the flow strength uncertainty is on the time-optimal paths.

3.2. Test Case 2: Stochastic double-gyre barotropic quasi-geostrophic circulation

We now consider stochastic time-optimal path planning for vehicles navigating in stochastic flow predictions from the stochastic DO level-set PDE simulations. For this test case, we simulate the idealized near-surface wind-driven barotropic quasi-geostrophic double-gyre ocean circulation at mid-latitudes, purposely similarly to Subramani and Lermusiaux [11], but now with uncertain barotropic initial conditions. The deterministic winds (e.g., mid-latitude easterlies and trade winds in the northern hemisphere) drive a zonal jet eastward (e.g., the Gulf Stream or Kuroshio) with a cyclonic gyre to its north and an anti-cyclonic gyre to its south. Such a circulation is governed by the following

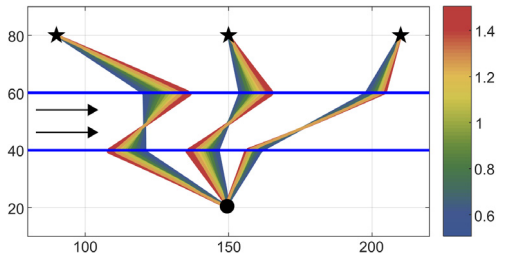

Fig. 6. *Stochastic time-optimal paths for Test Case 1:* All time-optimal paths are colored with the flow strength of the corresponding flow realization. The variability of the time-optimal paths is greatest for the target point upstream of the start point.

non-dimensional stochastic barotropic quasi-geostrophic model (e.g., [32,33]), written as conservation of momentum in the Langevin form,

$$\frac{\partial \mathbf{v}(\mathbf{x},t;\omega)}{\partial t} + \nabla\cdot(\mathbf{v}(\mathbf{x},t;\omega)\mathbf{v}(\mathbf{x},t;\omega)) + f\hat{k}\times\mathbf{v}(\mathbf{x},t;\omega) = -\nabla p(\mathbf{x},t;\omega) + \frac{1}{\mathrm{Re}}\nabla^2\mathbf{v}(\mathbf{x},t;\omega) + a\boldsymbol{\tau}\,, \tag{7a}$$

$$\nabla\cdot\mathbf{v}(\mathbf{x},t;\omega) = 0, \tag{7b}$$

$$\mathbf{v}(\mathbf{x},0;\omega) = \mathbf{v}_0(\mathbf{x};\omega), \tag{7c}$$

where Re is the Reynold's number, f is the Coriolis coefficient, and a is the strength of the wind stress. For the Coriolis coefficient, we employ a β-plane approximation $f = f_0 + \beta y$ with $f_0 = 0$. We utilize a horizontal length scale $L = 10^6$ m, vertical length scale $D = 10^3$ m, velocity scale $U = 1.98$ cm/s, time scale $T = 1.6$ yrs, density $\rho = 1025\,\mathrm{kg/m^3}$, stress scale $\tau_0 = 0.16$ MPa, eddy viscosity $A_H = 19.77\,\mathrm{m^2/s}$, and $\beta_0 = 1.977\times10^{-11}$ ms. This leads to non-dimensional numbers $\mathrm{Re} = \frac{UL}{A_H} = 1000$, $a = \frac{\tau_0 L}{\rho D U^2} = 1,000$, and $\beta = \beta_0 L^2/U = 1,000$. A deterministic non-dimensional steady zonal wind stress, $\boldsymbol{\tau} = \left[-\frac{1}{2\pi}\cos 2\pi y\ ,\ 0\right]^T$, forces the flow in the basin. The DO equations corresponding to the stochastic barotropic quasi-geostrophic dynamics Eq. (7) are provided in Appendix A.2.

We simulate the flow in a basin of size 1000 km × 1000 km by solving Eq. (A.8) and using the relevant numerical parameters in Table 2. The barotropic zonal and meridional velocities are initialized (Eq. (7c)) from a spatial correlation kernel with a length scale of 500 km and uniform variance. Five velocity DO modes and 5000 DO realizations are utilized (Table 2), and the simulation is spun-up for 1 non-dimensional time, i.e., 1.6 yrs. For path planning, we utilize the next 13.5 days of stochastic flow. We consider a vehicle with a nominal speed of 40 cm/s ([34], e.g.). Fig. 7 illustrates the DO mean, DO modes, and marginal PDF of the DO coefficients for the flow field at the beginning ($t = 0$ days) and end ($t = 13.5$ days) of the planning horizon.

Over the 13.5 day period, the mean flow is a strong zonal jet from east to west with a cyclonic gyre to the north of the jet and an anti-cyclonic gyre to the south (Fig. 7 Mean). From the variance of the coefficients (Fig. 7 Variance of Coeffs.), we see that Mode 1 has the most stochastic energy and explains the broad features of the uncertainty in the flow. Mode 1 has two zonal jets and three gyres (Fig. 7 Mode 1). The two jets are located north and south of the zonal jet of the mean. The stochastic coefficient corresponding to this mode has a bimodal distribution. For positive coefficients, the southern jet ($0.2 < y < 0.5$) contributes a flow from west to east and the northern jet ($0.5 < y < 0.8$) from east to west. For negative coefficients, the direction of this contribution is reversed. The northern and southern jets can be locally considered to be similar to the stochastic front crossing example (Test Case 1). Higher positive (negative) coefficients correspond to greater variation from the mean in the (opposite) direction of the modes. Modes 2–5 and their coefficients contribute to non-symmetric flow realizations (Fig. 7 Modes 2–5), such as the non-symmetric wind-driven gyres seen in the North Atlantic (e.g., [35,36]). Two realizations with most negative Coeff.1 (Realiz. #1) and with most positive Coeff. 1 (Realiz #5000) are shown in Fig. 8. Both these and 4998 other realizations are all simulated by one DO flow field simulation (Appendix A).

3.2.1. Analysis of stochastic reachability fronts and time-optimal paths

Now we plan stochastic time-optimal paths from a start point (0.2,0.2) to the target (0.4,0.8). Fig. 9 illustrates the evolution of stochastic reachability fronts (i.e., zero level-set contours) over the planning horizon, showing snapshots

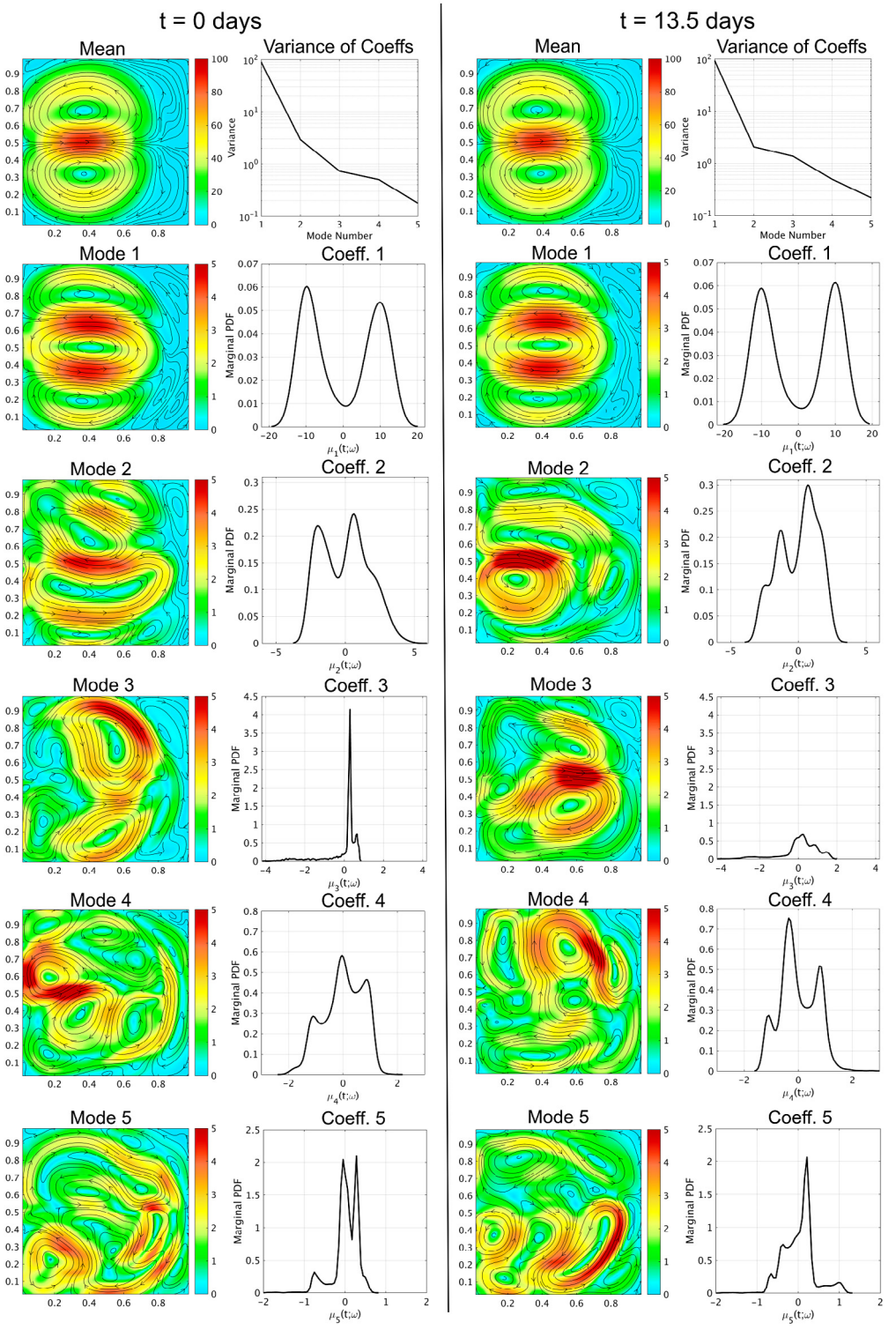

Fig. 7. *Stochastic flow field for Test Case 2:* The mean field and variance of the DO coefficients, then the 5 DO mode fields and the marginal PDF of the corresponding DO coefficients of the stochastic double-gyre flow field are shown at the beginning and end of the planning horizon. Streamlines are overlaid on a color plot of the flow magnitude (color axis in cm/s) for the DO mean and modes. The x- and y- axes have units of 1000 km. Realizations can be constructed by adding the mean to the sum of the product of each mode with a sample from the PDF of the corresponding coefficient.

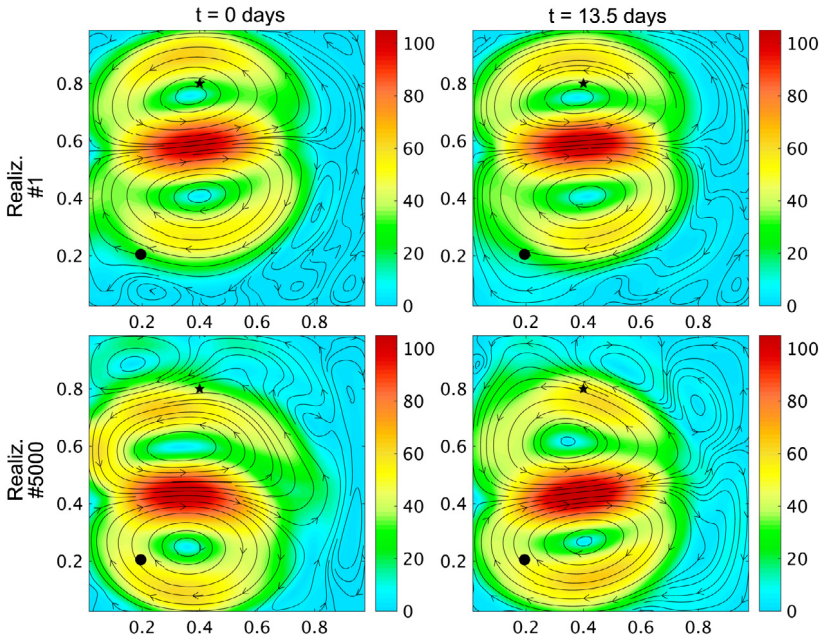

Fig. 8. *Two realizations of the stochastic flow field for Test Case 2:* Streamlines of the flow are overlaid on a color plot of the flow magnitude. Realiz. #1 corresponds to the most negative Coeff. 1 and realiz #5000 to the most positive Coeff. 1. All such realizations are integrated in time by one DO flow field simulation.

at nine discrete times. Each flow realization has a reachability front and all such fronts are computed by one DO simulation. Overall, the reachability front gets advected by the mean flow, but individual realizations experience the effect of the modes and coefficients of the flow. As such, the reachability fronts spread, leading to a density distribution (Fig. 9). The mean double-gyre advects the level-sets, and hence the reachability fronts are advected clockwise in the anti-cyclonic southern gyre and clockwise in the cyclonic northern gyre. To study the spread, we look at Fig. 9. Here, the reachability fronts are overlaid on streamlines of velocity DO mode 1, $\tilde{\mathbf{v}}_1(\mathbf{x}, t)$, and colored with velocity DO coefficient 1, $\mu_1(t;\omega)$. The initial spreading of the reachability fronts (Fig. 9b–d) in the southern part of the domain ($y < 0.5$) is due to the flow contribution by the southern jet of velocity DO mode 1. The reachability fronts corresponding to positive coefficients are advected to the east more than those corresponding to negative coefficients. The spreading of the reachability fronts in the northern part of the domain ($y > 0.5$) (Fig. 9f–i) is due to the flow contribution by the northern jet of velocity DO mode 1. Here, the effect on the reachability fronts is opposite to the effect due to the southern jet, i.e., more positive coefficients are advected to the west more than the realizations corresponding to more negative coefficients. The spread of the reachability fronts in the strong mean zonal jet (approximately $0.45 < y < 0.55$) is not affected much, as the contribution to the flow by all velocity modes in this region is weak (Fig. 9c–f). The finer details in the shape of the reachability fronts are due to contributions of the velocity modes with lower stochastic energy (modes 2–5).

Next, we study the spatial distribution of the time-optimal paths (Fig. 10). In Fig. 10a, each path is colored with the corresponding flow realization's velocity DO coefficient 1, $\mu_1(t;\omega)$. In Fig. 10b, each path is colored with the arrival-time for that path. All paths cross the strong mean zonal jet by *riding* the anti-cyclonic southern gyre first and then the cyclonic northern gyre. The spread in the paths is a result of the variability in the reachability fronts as described above. The most negative coefficient $\mu_1(t;\omega)$ defines the western edge of the spatial distribution of paths and the most positive $\mu_1(t;\omega)$ defines the eastern edge as seen in Fig. 10a. When paths are colored by the arrival time (Fig. 10b), one sees that the arrival time for paths that are very different spatially (and corresponding to different flow realizations) can be nonetheless similar. This is due to the complex PDF of the stochastic velocity field. In this test case, the arrival time range varies from 12.1 to 13.6 days. For reference, under no flow conditions, a vehicle with a speed of 40 cm/s would take 18.3 days to travel between the start and target points considered in this test case 2.

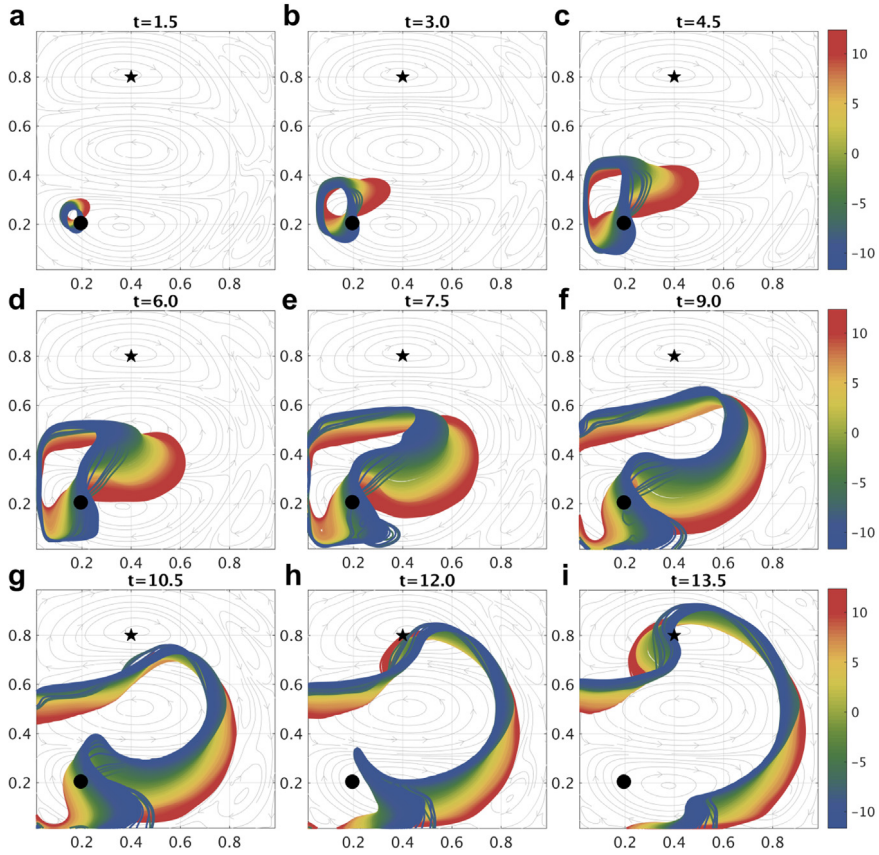

Fig. 9. *Stochastic reachability fronts for Test Case 2:* The reachability front for each of the flow realizations is colored with its corresponding velocity DO coefficient 1, $\mu_1(t;\omega)$. Time t is in days, and x- and y- axes are in thousands of km.

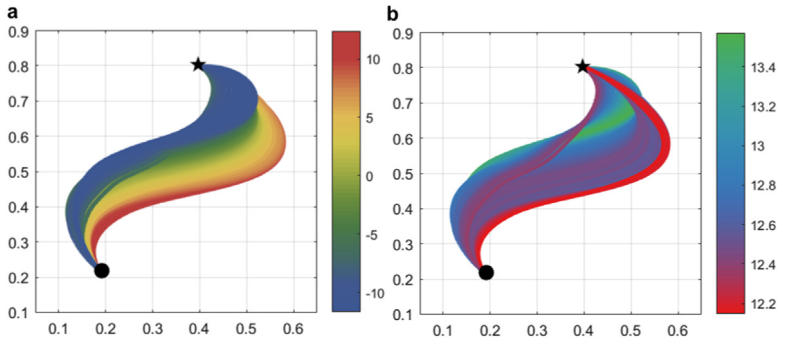

Fig. 10. *Stochastic time-optimal paths for Test Case 2:* The time-optimal paths are colored with (a) the velocity DO coefficient 1, $\mu_1(t;\omega)$, and (b) the arrival time (in days) at the target shown. x- and y- axes are in thousands of km.

The examples so far also show that the time-optimal path can be very sensitive to the uncertainty in the flow field. A strength of the stochastic DO level-set equations is that they allow the rigorous prediction of this sensitivity in a computationally efficient manner. The examples also raise the need of computing risk-optimal paths in uncertain flows, a topic addressed in [37].

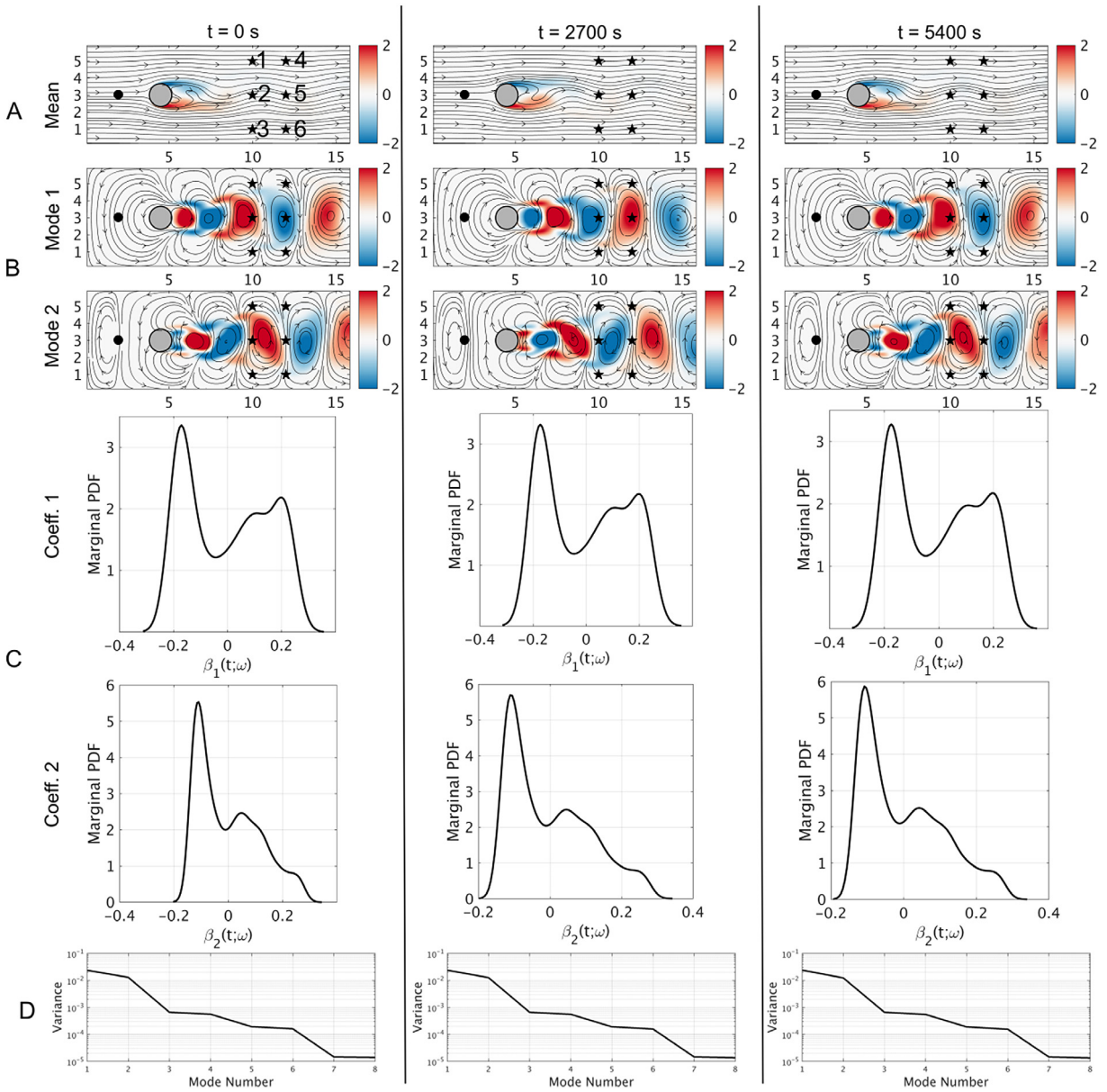

Fig. 11. *Flow field for Test Case 3:* Row A shows the DO mean flow, with streamlines overlaid on colored vorticity. Row B shows the same for mode 1 and mode 2 fields. Row C shows the marginal PDF of coefficients 1 and 2. Row D shows the decay in variance of the first eight modes. Each column is a snapshot, at the time specified at the top. The starting point of the propelled vehicle is indicated by a circular marker and the 6 targets by star markers.

3.3. Test Case 3: Stochastic flow past a circular island

In the third test case, we consider time-optimal path planning in a stochastic flow behind a circular island in a channel. Fig. 11 shows the domain and flow configuration (vorticity overlaid with streamlines). The flow is governed by the stochastic barotropic quasi-geostrophic Eq. (7c), but with $f = 0$ and $\boldsymbol{\tau} = [0\,,\,0]^T$. We model a channel 16 km $\times$ 6 km with a circular island of diameter 1 km. Here, we utilize a turbulent eddy viscosity $A_H = 10$ m^2/s, length scale $L = 1$ km, velocity scale $U = 1$ m/s, and time scale $T = 1000$ s, leading to a non-dimensional

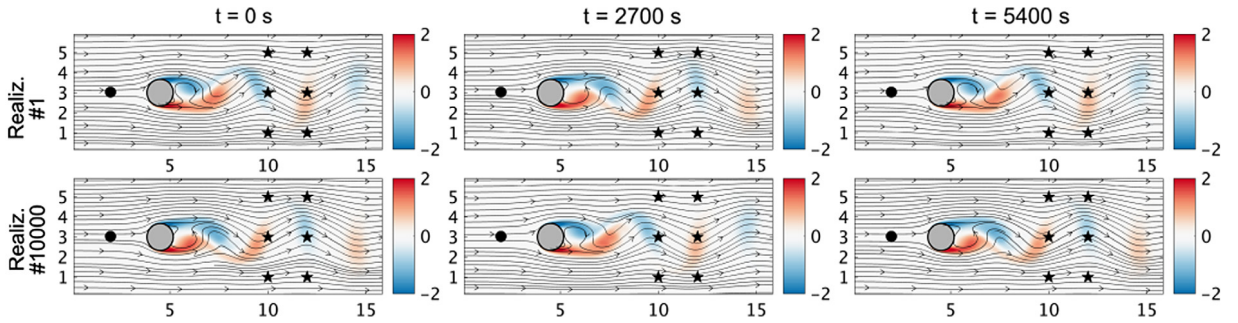

Fig. 12. *Two realizations of the stochastic flow field for Test Case 3:* Streamlines are overlaid on a color plot of vorticity. Realiz. #1 corresponds to the most negative Coeff. 1 while realiz. #10,000 to the most positive Coeff. 1. All such realizations are integrated in time by one DO flow field simulation.

Reynold's number of 100. We consider a deterministic barotropic inlet into the channel of $\mathbf{v} = [1\ ,\ 0]^T$ m/s on the western boundary. The northern and southern boundaries have free-slip wall conditions and the eastern boundary has open conditions. The barotropic initial conditions are generated from a covariance kernel with a spatial correlation length scale of 5 km in the zonal direction and 2 km in the meridional direction. 8 velocity DO modes and 10,000 DO realizations are employed here (Table 2). The simulation is spun-up until stochastic eddies are generated downstream from the island. Then, the flow for 1.5 h (non-dimensional time of 5.4) is considered for path planning.

Fig. 11 shows the velocity mean (row A), the first two velocity DO modes (row B), marginal PDF of the corresponding DO coefficients (row C), and the variance of first eight DO modes (row D). Each column of Fig. 11 shows the above quantities at $t = 0$, 2700, and 5400 s. From the decay in variance (row D), we see that most of the flow uncertainty is captured by the DO modes 1 and 2, and hence other modes and coefficients are not shown (but we used 8 modes). The mean flow accelerates to the south and north of the island as it is confined by the channel and has almost zero magnitude in the lee just behind the island. The stochastic initial conditions result in uncertainty in the eddy strength, shedding frequency, and whether the eddies are first shed to the north or south of the island. The modes 1 and 2 have eddies downstream from the island which together with the coefficients explain the uncertainty in the flow downstream.

Fig. 12 shows two realizations corresponding to the most negative (Realiz. #1) and positive (Realiz. #10,000) coeff. 1. We see that in Realiz. #1, eddies shed to the north of the island while for realiz. #10,000, they shed to the south of the island.

3.3.1. Analysis of stochastic reachability fronts and time-optimal paths

Now we plan stochastic time-optimal paths for navigating a propelled vehicle with a nominal speed of 1 m/s from a start point (2,3) upstream of the island to six possible target points (see Figs. 11–12: the start point is indicated by circular markers and targets by star markers). Fig. 13 shows the evolution of the stochastic reachability front overlaid on streamlines of velocity modes 1 (column A) and 2 (column B). In each plot, we color the reachability fronts with their respective coefficients. The level-sets do not grow west of the start point as the vehicle speed and the mean flow there are equal and opposite, making the reachability front stationary at the start point. Until $t = 1800$ s, the reachability fronts for all flow realizations are almost identical as the flow uncertainty in the reachable sets is insignificant (Fig. 13A.i, B.i). The shape of the reachability fronts is set by the mean flow between $t = 1800$ and 2400 s. The reachability front grows normal to itself at the nominal vehicle speed in the close-to-zero mean flow region behind the cylinder (Fig. 13A.ii, B.ii). After $t = 1800$ s, the spreading of the reachability fronts due to the effect of velocity DO modes start. The mean flow advects all the reachability fronts to the east. From $t = 3000$ s, the reachability fronts start splitting into two groups roughly corresponding to positive and negative values of coefficient 1. At $t = 3600$ s, the group of reachability fronts with positive coefficient 1 have a kink near $y = 3.5$ and those with negative coefficient 1 have a kink near $y = 2.5$ corresponding to the eddy direction (Fig. 13A.iv). At $t = 4500$ s, the reachability fronts have two groups corresponding to positive and negative coefficient 2 (Fig. 13A.v). At $t = 5400$ s, the behavior is similar to $t = 3600$ s, with two distinct groups of reachability fronts corresponding to positive and negative values of coefficient 1.

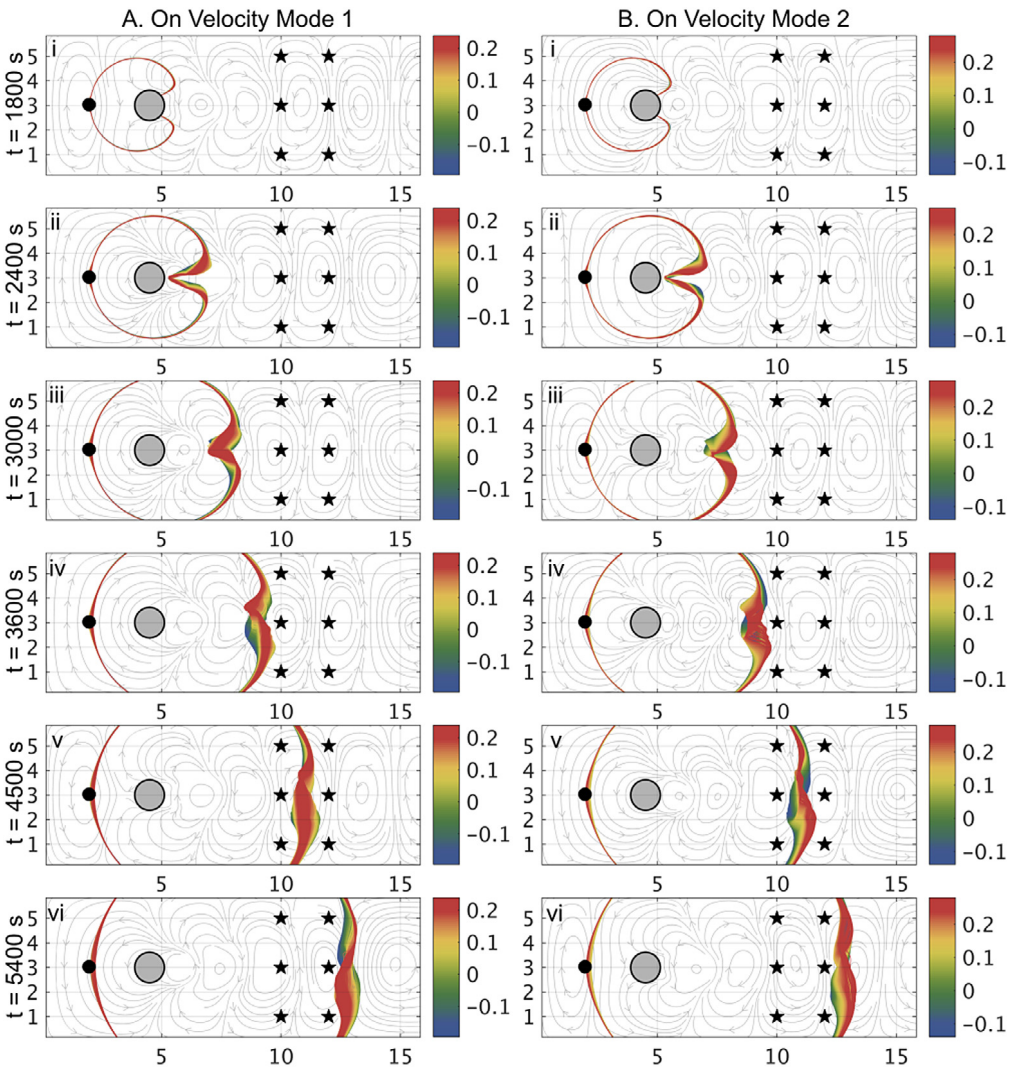

Fig. 13. *Stochastic reachability fronts for Test Case 3:* In column A (B) the reachability fronts are overlaid on the velocity streamlines of Mode 1 (2) and colored by coefficient 1 (2). Rows i–vi are snapshots at the indicated times. Starting point of the propelled vehicle is indicated by a circular marker and the six possible targets by star markers.

Next, we study the spatial distribution of the time-optimal paths (Fig. 14). In Fig. 14, column A has all paths colored with velocity coefficient 1, and column B has all paths colored with velocity coefficient 2. Row *i* has all paths to target 2, row *ii* to target 5, and row *iii* to all other targets. Paths to targets 1, 3, 4, and 6 (row *iii*) have little variance, since these paths are mostly outside the regions of flow uncertainty. Paths to target 5 (row *ii*) have the maximum variance followed by paths to target 2 (row *i*), as these are affected by the flow uncertainty. There are two sets of paths: one set that goes north of the island and another that goes south. The combination of velocity modes and coefficients creates flow realizations that lead to northern paths or southern paths. This bifurcation mirrors the uncertainty in eddy shedding downstream from the island. An error in estimating the direction of eddy shedding will result in large errors in the time-optimal path predictions to targets 2 and 5 (e.g., north vs. south) for this test case. However, predictions to targets 1, 3, 4, and 6 are largely unaffected by such an error. This illustration quantitatively confirms the fact that sensitivity of path predictions depends not only on the flow itself but also on the target locations, and all such paths and sensitivities can be computed by solving our equations. Notably, an advantage of our methodology is that only

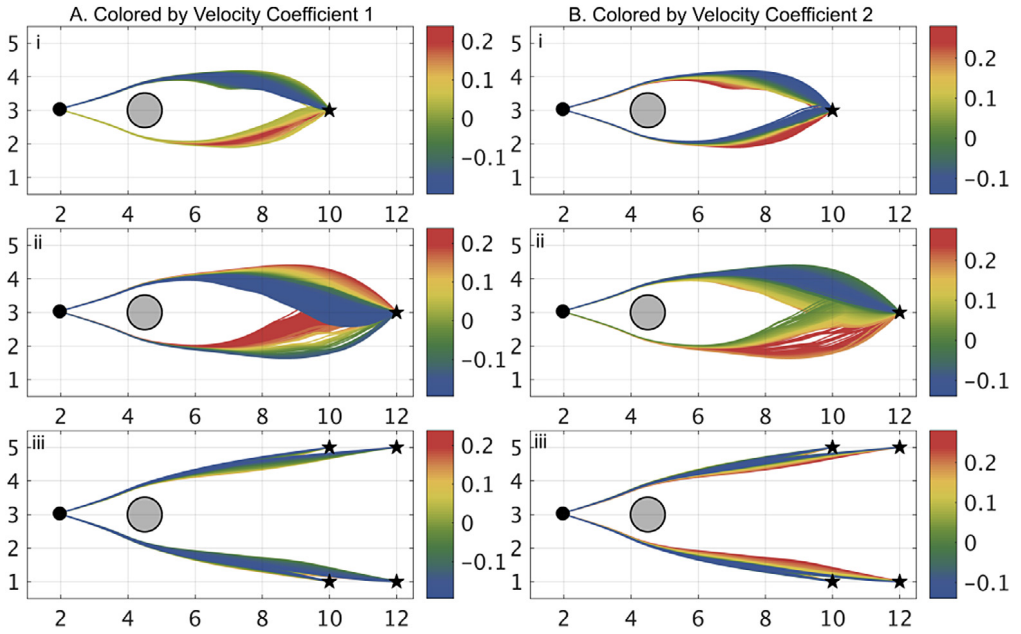

Fig. 14. *Stochastic time-optimal paths for Test Case 3:* Column A (B) has paths colored by velocity coefficient 1 (2). Row *i* shows all paths to target 2, row *ii* to target 5, and row *iii* to the other 4 targets. The $x-$ and $y-$ axes are in kms.

one reachability front simulation is required for one start location and start time. The paths to multiple targets are obtained by solving the backtracking stochastic ODE Eq. (2), which is very inexpensive to solve.

Fig. 15 shows the distribution of arrival times at the six targets. As expected from the distributions of time-optimal paths, the distributions of arrival times at targets 1, 3, 4, and 6 are tighter compared to other two targets. Target 5 indeed has the most variance in arrival time, and the distribution is bimodal similar to the bimodal distribution of velocity DO coefficients 1 and 2.

4. Conclusion

We obtained and applied fundamental equations for time-optimal path planning in uncertain, dynamic and strong flows. We first presented the stochastic level-set PDEs that govern the exact evolution of reachability fronts for vehicles navigating in uncertain, strong, and dynamic flow fields. We then developed efficient stochastic dynamically orthogonal level-set PDEs that solve the above equations in a reduced dynamic subspace, providing several orders of magnitude computational speed-up when compared to direct Monte Carlo methods. To compute stochastic time-optimal paths, we utilized the governing stochastic particle backtracking ODE. We then applied the equations to compute stochastic reachability fronts and time-optimal paths in three different scenarios: a steady-front of uncertain strength, a stochastic double-gyre circulation, and a stochastic flow past a circular island. We utilized the first test case to verify that our DO level-set equations can compute the distribution of stochastic reachability fronts and time-optimal paths as accurately as traditional Monte Carlo methods. In the second case, we quantitatively explained the effect of the first DO velocity mode (with the most stochastic energy) on setting the shape and distribution of the reachability fronts and time-optimal paths. We also showed that the paths corresponding to different flow realizations can have large spatial differences but similar arrival times, due to the complex PDF of the stochastic velocity fields. In the third case, we described how the variance of time-optimal paths and arrival times depended mostly on the first two DO velocity modes. We showed that the variability could be large due to the uncertainty in estimating the direction of eddy shedding for targets directly downstream of an island. Importantly, all these paths are computed by one simulation of the stochastic DO level-set equations.

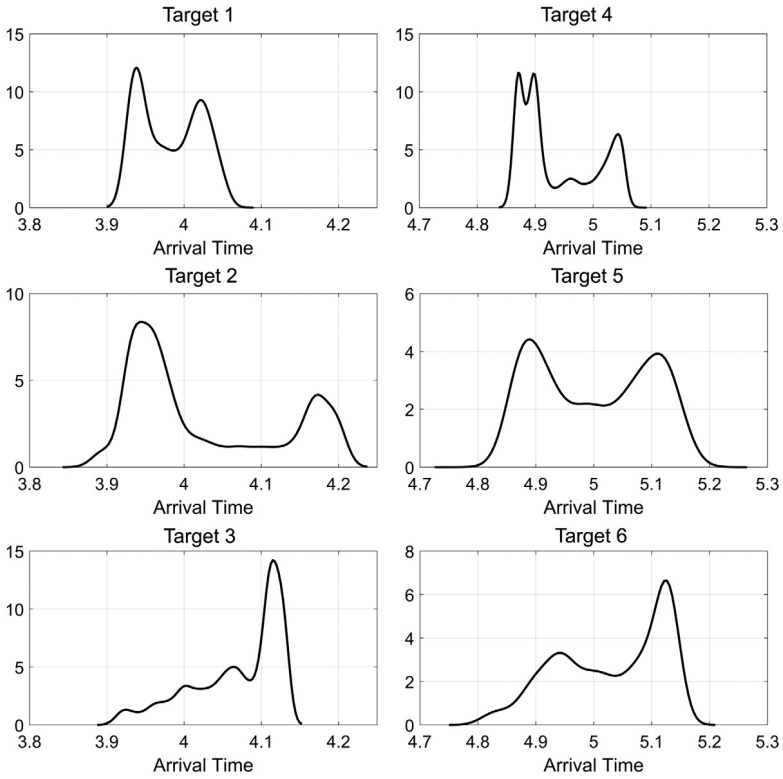

Fig. 15. *Arrival time distribution at each of the six targets for Test Case 3:* The distribution at targets 1 and 4, 2 and 5, and 3 and 6, are similar, respectively. The distributions at targets 1 and 3, and targets 4 and 6 are almost mirror images due to their symmetric spatial location north and south of the circular island, respectively.

Overall, our analysis offers insights into the behavior of vehicles navigating in canonical uncertain flows often encountered in coastal ocean regions. In addition to computing stochastic reachability fronts and time-optimal paths, the new equations provide a rigorous framework for quantifying the sensitivity of time-optimal paths to variability and errors in flow field predictions. In the future, our methodology can be applied with realistic uncertainty flow predictions (e.g., [16,38,39]). The stochastic DO level-set equations can be augmented with decision theory to compute risk-optimal paths for vehicles navigating in uncertain flow fields. Even though we emphasized the navigation of autonomous vehicles in ocean flows, the methodology and equations are general: they can be utilized for aerial vehicles, land robots, or ships (e.g., [40]).

Acknowledgments

We thank the members of our MSEAS group for useful discussions, especially Mr. Chinmay Kulkarni and Mr. Arkopal Dutt for their feedback on the manuscript. We also thank the MIT-Tata Center Program for the Fellowship support of DNS. We are grateful to the Office of Naval Research (ONR) for research support under grants N00014-14-1-0476 (Science of Autonomy-LEARNS) and N00014-15-1-2616 (NASCar-OPS) to the Massachusetts Institute of Technology (MIT).

Appendix A

In this appendix, we first outline generic Dynamically Orthogonal field equations and then provide the barotropic quasi-geostrophic DO equations. We refer to Table 1 for the notation.

A.1. Generic DO equations

Prior to describing the Dynamically Orthogonal field equations [26,27,41], we first provide some definitions. For any two fields $\tilde{\psi}_1(\mathbf{x}, t)$ and $\tilde{\psi}_2(\mathbf{x}, t)$, the spatial inner product is defined as

$$\left\langle \tilde{\psi}_1(\bullet, t), \tilde{\psi}_2(\bullet, t) \right\rangle = \int_D \tilde{\psi}_1(\mathbf{x}, t)^T \tilde{\psi}_2(\mathbf{x}, t)\, \mathrm{d}\mathbf{x}\,, \tag{A.1}$$

the orthogonal component operator as

$$\Gamma^{\perp}_{\tilde{\psi}} G(\mathbf{x}) = G(\mathbf{x}) - \sum_{k=1}^{n_{s,\psi}} \left\langle G(\bullet), \tilde{\psi}_k(\bullet, t) \right\rangle \tilde{\psi}_k(\mathbf{x}, t)\,, \tag{A.2}$$

and the expectation operator as

$$\mathbb{E}[\psi(\mathbf{x}, t; \omega)] = \int_{\Omega} \psi(\mathbf{x}, t; \omega) \mathrm{d}\mathcal{P}(\omega)\,. \tag{A.3}$$

Consider the time evolution of a general stochastic continuous field $\psi(\mathbf{x}, t; \omega)$ (e.g., $\psi(\mathbf{x}, t; \omega) = \phi(\mathbf{x}, t; \omega)$ for the level-set scalar field and $\psi(\mathbf{x}, t; \omega) = \mathbf{v}(\mathbf{x}, t; \omega)$ for the velocity vector field), described by a S-PDE

$$\frac{\partial \psi(\mathbf{x}, t; \omega)}{\partial t} = \mathcal{L}[\psi(\mathbf{x}, t; \omega), \mathbf{x}, t; \omega]\,, \tag{A.4}$$

where $\mathcal{L}$ is a general nonlinear operator. Introducing a generalized dynamic Karhunen–Loeve (KL) decomposition (a DO decomposition)

$$\psi(\mathbf{x}, t; \omega) = \bar{\psi}(\mathbf{x}, t) + \sum_{i=0}^{n_{s,\psi}} Y_i(t; \omega) \tilde{\psi}_i(\mathbf{x}, t)\,, \tag{A.5}$$

into (Eq. (A.4)), applying the expectation (Eq. (A.3)) and spatial inner-product (Eq. (A.1)) operators, and an orthogonality condition on the evolution of the stochastic subspace,

$$\left\langle \frac{\partial \tilde{\psi}_i}{\partial t}, \tilde{\psi}_j \right\rangle = 0 \qquad \forall\, i, j\,, \tag{A.6}$$

we obtain the DO equations for the statistical mean $\bar{\psi}$, stochastic coefficients Y_i, and deterministic modes $\tilde{\psi}_i$ as

$$\frac{\partial \bar{\psi}(\mathbf{x}, t)}{\partial t} = \mathbb{E}[\mathcal{L}]\,, \tag{A.7a}$$

$$\frac{\partial Y_i(t; \omega)}{\partial t} = \left\langle \mathcal{L} - \mathbb{E}[\mathcal{L}], \tilde{\psi}_i \right\rangle\,, \tag{A.7b}$$

$$\frac{\partial \tilde{\psi}_i(\mathbf{x}, t)}{\partial t} = \sum_{j=1}^{n_{s,\psi}} C^{-1}_{ij} \Gamma^{\perp}_{\tilde{\psi}} \mathbb{E}[Y_j \mathcal{L}]\,, \tag{A.7c}$$

where we have dropped $(\mathbf{x}, t)$ from the inner-product terms for brevity of notation. Here, the $n_{s,\psi}$ modes $\tilde{\psi}_i$ and stochastic coefficients Y_i are dynamic and governed by differential equations, distinguishing them from classic empirical orthogonal functions and proper orthogonal decomposition approaches. These dynamic modes describe an evolving subspace, and the coefficients evolve the uncertainty within that dynamic subspace. For nonlinear dynamical systems, the intrinsic nonlinearities in Eq. (A.4) and the corresponding dynamics retained in Eqs. (A.7a)–(A.7c) often enable truncating the number of $n_{s,\psi}$ modes and coefficients to a much smaller number than the dimensions (spatial and stochastic) of the original discretization of Eq. (A.4). It is this dynamics and the adaptable size $n_{s,\psi}$ that allow the DO equations to accurately capture most of the stochasticity of the original variables [27,42,43].

A.2. Dynamically orthogonal quasi-geostrophic equations

In this appendix, we provide the Dynamically Orthogonal barotropic Quasi-Geostrophic equations that we utilized to generate stochastic flow fields. Detailed description of similar equations for Boussinesq dynamics, their derivation

and numerical schemes are provided in [41] and the implementation is provided in [44]. The equations for the DO mean (Eqs. (A.8a), (A.8b)), coefficients (Eq. (A.8c)), and modes (Eqs. (A.8d), (A.8e)) of the S-PDE (7) are

$$\nabla \cdot \bar{\mathbf{v}} = 0\,, \tag{A.8a}$$

$$\frac{\partial \bar{\mathbf{v}}}{\partial t} = \frac{1}{Re}\nabla^2 \bar{\mathbf{v}} - \nabla \cdot (\bar{\mathbf{v}}\bar{\mathbf{v}}) - C_{\mu_m \mu_n} \nabla \cdot (\tilde{\mathbf{v}}_m \tilde{\mathbf{v}}_n) - f\hat{k} \times \bar{\mathbf{v}} - \nabla \bar{p} + a\boldsymbol{\tau}\,, \tag{A.8b}$$

$$\begin{aligned} \frac{\mathrm{d}\mu_i}{\mathrm{d}t} &= \mu_m \left\langle \frac{1}{Re}\nabla^2 \tilde{\mathbf{v}}_m - \nabla \cdot (\tilde{\mathbf{v}}_m \bar{\mathbf{v}}) - \nabla \cdot (\bar{\mathbf{v}}\tilde{\mathbf{v}}_m) - \nabla \tilde{p}_m - f\hat{k} \times \tilde{\mathbf{v}}_m, \tilde{\mathbf{v}}_i \right\rangle \\ &\quad - (\mu_m \mu_n - C_{\mu_m \mu_n}) \left\langle \nabla \cdot (\tilde{\mathbf{v}}_m \tilde{\mathbf{v}}_n), \tilde{\mathbf{v}}_i \right\rangle\,, \end{aligned} \tag{A.8c}$$

$$\nabla \cdot \tilde{\mathbf{v}}_i = 0\,, \tag{A.8d}$$

$$\frac{\partial \tilde{\mathbf{v}}_i}{\partial t} = \mathbf{Q}^{\mathbf{v}}{}_i - \left\langle \mathbf{Q}^{\mathbf{v}}{}_i, \tilde{\mathbf{v}}_k \right\rangle \tilde{\mathbf{v}}_k\,, \tag{A.8e}$$

$$\text{where } \mathbf{Q}^{\mathbf{v}}{}_i = \frac{1}{Re}\nabla^2 \tilde{\mathbf{v}}_i - \nabla \cdot (\tilde{\mathbf{v}}_i \bar{\mathbf{v}}) - \nabla \cdot (\bar{\mathbf{v}}\tilde{\mathbf{v}}_i) - \nabla \tilde{p}_i - C^{-1}_{\mu_i \mu_j} M_{\mu_j \mu_m \mu_n} \nabla \cdot (\tilde{\mathbf{u}}_m \tilde{\mathbf{u}}_n)\,,$$

where we have dropped the parenthesis $(\mathbf{x}, t; \omega)$ for brevity of notation. We solved Eqs. (A.8) to obtain the stochastic flow fields utilized in Test Cases 2 and 3 of the present paper (Section 3).

References

[1] J.G. Bellingham, K. Rajan, Robotics in remote and hostile environments, Science 318 (5853) (2007) 1098–1102.

[2] T.B. Curtin, J.G. Bellingham, Progress toward autonomous ocean sampling networks, Deep-Sea Res. II 56 (3) (2009) 62–67.

[3] O. Schofield, S. Glenn, J. Orcutt, M. Arrott, M. Meisinger, A. Gangopadhyay, W. Brown, R. Signell, M. Moline, Y. Chao, S. Chien, D. Thompson, A. Balasuriya, P.F.J. Lermusiaux, M. Oliver, Automated sensor networks to advance ocean science, EOS Trans. AGU 91 (39) (2010) 345–346. http://dx.doi.org/10.1029/2010EO390001.

[4] P.F.J. Lermusiaux, Uncertainty estimation and prediction for interdisciplinary ocean dynamics, J. Comput. Phys. 217 (1) (2006) 176–199. http://dx.doi.org/10.1016/j.jcp.2006.02.010.

[5] Y.K. Hwang, N. Ahuja, Gross motion planning –a survey, ACM Comput. Surv. 24 (3) (1992) 219–291.

[6] S.M. LaValle, Planning Algorithms, Cambridge University Press, Cambridge, UK, 2006.

[7] T. Lolla, P.F.J. Lermusiaux, M.P. Ueckermann, Jr., P.J. Haley, Time-optimal path planning in dynamic flows using level set equations: theory and schemes, Ocean Dyn. 64 (10) (2014) 1373–1397. http://dx.doi.org/10.1007/s10236-014-0757-y.

[8] P.F.J. Lermusiaux, D.N. Subramani, J. Lin, C.S. Kulkarni, A. Gupta, A. Dutt, T. Lolla, P.J. Haley Jr., W.H. Ali, C. Mirabito, S. Jana, A future for intelligent autonomous ocean observing systems, in: The Sea, vol. 17, 2017. The Science of Ocean Prediction, Part 2, Special Issue, J. Marine Res. 75, in press.

[9] T. Lolla, M.P. Ueckermann, K. Yiğit, P.J. Haley Jr., P.F.J. Lermusiaux, Path planning in time dependent flow fields using level set methods,in: International Conference on Robotics and Automation, ICRA, 14–18 May 2012, 2012, pp. 166–173, http://dx.doi.org/10.1109/ICRA.2012.6225364.

[10] T. Lolla, P.J. Haley Jr., P.F.J. Lermusiaux, Path planning in multiscale ocean flows: coordination and dynamic obstacles, Ocean Model. 94 (2015) 46–66. http://dx.doi.org/10.1016/j.ocemod.2015.07.013.

[11] D.N. Subramani, P.F.J. Lermusiaux, Energy-optimal path planning by stochastic dynamically orthogonal level-set optimization, Ocean Model. 100 (2016) 57–77. http://dx.doi.org/10.1016/j.ocemod.2016.01.006.

[12] W. Sun, P. Tsiotras, T. Lolla, D.N. Subramani, P.F.J. Lermusiaux, Pursuit-evasion games in dynamic flow fields via reachability set analysis, in: 2017 American Control Conference, ACC, Seattle, 2017, pp. 4595–4600, http://dx.doi.org/10.23919/ACC.2017.7963664.

[13] W. Sun, P. Tsiotras, T. Lolla, D.N. Subramani, P.F.J. Lermusiaux, Multiple-pursuer-one-evader pursuit evasion game in dynamic flow fields, J. Guid. Control Dyn. 40 (7) (2017). http://dx.doi.org/10.2514/1.G002125.

[14] T. Lolla, P.J. Haley Jr., P.F.J. Lermusiaux, Time-optimal path planning in dynamic flows using level set equations: Realistic applications, Ocean Dyn. 64 (10) (2014) 1399–1417. http://dx.doi.org/10.1007/s10236-014-0760-3.

[15] D.N. Subramani, P.J. Haley Jr., P.F.J. Lermusiaux, Energy-optimal path planning in the coastal ocean, J. Geophys. Res. Oceans 122 (2017) 3981–4003. http://dx.doi.org/10.1002/2016JC012231.

[16] D.N. Subramani, P.F.J. Lermusiaux, P.J. Haley Jr., C. Mirabito, S. Jana, C.S. Kulkarni, A. Girard, D. Wickman, J. Edwards, J. Smith, Time-optimal path planning: Real-time sea exercises, in: Oceans '17 MTS/IEEE Conference, Aberdeen, 2017, http://dx.doi.org/10.1109/OCEANSE.2017.8084817.

[17] M.P. Wellman, M. Ford, K. Larson, Path planning under time-dependent uncertainty, in: Proceedings of the Eleventh Conference on Uncertainty in Artificial Intelligence, UAI'95, Morgan Kaufmann Publishers Inc., San Francisco, CA, USA, 1995, pp. 532–539. URL http://dl.acm.org/citation.cfm?id=2074158.2074219.

[18] G. Kewlani, G. Ishigami, K. Iagnemma, Stochastic mobility-based path planning in uncertain environments, in: 2009 IEEE/RSJ International Conference on Intelligent Robots and Systems, Oct. 2009, pp. 1183–1189.
[19] J. Barraquand, J.-C. Latombe, A Monte-Carlo algorithm for path planning with many degrees of freedom, in: Proceedings of IEEE International Conference on Robotics and Automation, IEEE, Cincinnati, OH, USA, 1990, pp. 1712–1717.
[20] D. Rathbun, S. Kragelund, A. Pongpunwattana, B. Capozzi, An evolution based path planning algorithm for autonomous motion of a UAV through uncertain environments, in: Digital Avionics Systems Conference, 2002. Proceedings. The 21st, Vol. 2, pp. 8D2–1–8D2–12 vol.2.
[21] T. Wang, O.P. Le Maître, I. Hoteit, O.M. Knio, Path planning in uncertain flow fields using ensemble method, Ocean Dyn. 66 (10) (2016) 1231–1251.
[22] D. Xiu, G.E. Karniadakis, The Wiener–Askey polynomial chaos for stochastic differential equations, SIAM J. Sci. Comput. 24 (2) (2002) 619–644.
[23] R.G. Ghanem, P.D. Spanos, Stochastic Finite Elements: A Spectral Approach, Dover Publications, Mineola, NY, 2003.
[24] B.J. Debusschere, H.N. Najm, P.P. Pébay, O.M. Knio, R.G. Ghanem, O.P. Le Maître, Numerical challenges in the use of polynomial chaos representations for stochastic processes, SIAM J. Sci. Comput. 26 (2) (2004) 698–719.
[25] M.P. Pettersson, G. Iaccarino, J. Nordström, Polynomial chaos methods, in: Polynomial Chaos Methods for Hyperbolic Partial Differential Equations, Springer, 2015, pp. 23–29.
[26] T.P. Sapsis, P.F.J. Lermusiaux, Dynamically orthogonal field equations for continuous stochastic dynamical systems, Physica D 238 (23–24) (2009) 2347–2360. http://dx.doi.org/10.1016/j.physd.2009.09.017.
[27] T.P. Sapsis, P.F.J. Lermusiaux, Dynamical criteria for the evolution of the stochastic dimensionality in flows with uncertainty, Physica D 241 (1) (2012) 60–76. http://dx.doi.org/10.1016/j.physd.2011.10.001.
[28] F. Feppon, P.F.J. Lermusiaux, A geometric approach to dynamical model-order reduction, SIAM J. Matrix Anal. Appl. (2018) in press.
[29] Q.J. Wei, Time-Optimal Path Planning in Uncertain Flow Fields Using Stochastic Dynamically Orthogonal Level Set Equations (Bachelors thesis), Massachusetts Institute of Technology, Department of Mechanical Engineering, Cambridge, Massachusetts, 2015.
[30] H. Alt, M. Godau, Computing the Fréchet distance between two polygonal curves, Int. J. Comput. Geom. Appl. 5 (01n02) (1995) 75–91.
[31] Z. Danziger, MATLAB code for calculating discrete frechet distance, 2011. http://www.mathworks.com/matlabcentral/fileexchange/31922-discrete-frechet-distance. Online; (Accessed 8 August 2014).
[32] J. Pedlosky, Ocean Circulation Theory, Springer-Verlag, Berlin, 1998.
[33] B. Cushman-Roisin, J. Beckers, Introduction to Geophysical Fluid Dynamics. Physical and Numerical Aspects, Vol. 101, Academic Press, Waltham, MA, 2011.
[34] D.L. Rudnick, R.E. Davis, C.C. Eriksen, D.M. Fratantoni, M.J. Perry, Underwater gliders for ocean research, Mar. Technol. Soc. J. 38 (2) (2004) 73–84.
[35] A. Gangopadhyay, A. Robinson, Circulation and dynamics of the western North Atlantic. Part III: Forecasting the meanders and rings, J. Atmos. Ocean. Technol. 14 (6) (1997) 1352–1365.
[36] H.A. Dijkstra, M.J. Molemaker, Imperfections of the North Atlantic wind-driven ocean circulation: Continental geometry and windstress shape, J. Mar. Res. 57 (1) (1999) 1–28.
[37] D.N. Subramani, P.F.J. Lermusiaux, Risk-optimal path planning in uncertain, strong and dynamic flows, 2018, in preparation.
[38] P.F.J. Lermusiaux, P.J. Haley Jr., S. Jana, A. Gupta, C.S. Kulkarni, C. Mirabito, W.H. Ali, D.N. Subramani, A. Dutt, J. Lin, A.Y. Shcherbina, C.M. Lee, A. Gangopadhyay, Optimal planning and sampling predictions for autonomous and Lagrangian platforms and sensors in the northern Arabian Sea, Oceanography 30 (2) (2017) 172–185. http://dx.doi.org/10.5670/oceanog.2017.242.
[39] D.N. Subramani, Probabilistic Regional Ocean Predictions: Stochastic Fields and Optimal Planning (Ph.D. thesis), Massachusetts Institute of Technology, Department of Mechanical Engineering, Cambridge, Massachusetts, 2018.
[40] G. Mannarini, N. Pinardi, G. Coppini, P. Oddo, A. Iafrati, VISIR-I: Small vessels–least-time nautical routes using wave forecasts, Geosci. Model Dev. 9 (4) (2016) 1597–1625.
[41] M.P. Ueckermann, P.F.J. Lermusiaux, T.P. Sapsis, Numerical schemes for dynamically orthogonal equations of stochastic fluid and ocean flows, J. Comput. Phys. 233 (2013) 272–294. http://dx.doi.org/10.1016/j.jcp.2012.08.041.
[42] P.F.J. Lermusiaux, Estimation and study of mesoscale variability in the strait of Sicily, Dyn. Atmos. Oceans 29 (2) (1999) 255–303. http://dx.doi.org/10.1016/s0377-0265(99)00008-1.
[43] F. Feppon, P.F.J. Lermusiaux, Dynamically orthogonal numerical schemes for efficient stochastic advection and Lagrangian transport, SIAM Rev. (2018) in press.
[44] M.P. Ueckermann, P.F.J. Lermusiaux, 2.29 Finite Volume MATLAB Framework Documentation. MSEAS Report 14, Department of Mechanical Engineering, Massachusetts Institute of Technology, Cambridge, MA, 2012. URL http://mseas.mit.edu/?p=2567.